The Effect of Variant Selection on Texture of TWIP/TRIP Steels During Uniaxial Tensile Loading

MARTON BENKE, ADRIENN HLAVACS, ERZSEBET NAGY, GABOR KARACS, and VALERIA MERTINGER

The aim of the present manuscript is to reveal the role of variant selection associated with the $\gamma \rightarrow \varepsilon$ and $\gamma \rightarrow \varepsilon \rightarrow \alpha'$ transformations in the resulting texture of γ, ε and α' phases of FeMnCr steels during uniaxial loading. Tensile tests were carried out at temperatures well above and close to the martensite start temperature of the ε phase (M_S^{ε}). Pole figures were obtained from the cross-section of the fractured specimens by X-ray diffraction (XRD). The γ $\langle 111 \rangle$ texture developed regardless of test temperature. It was found that the ratio of diffracted intensity in the 0 and ~ 70 deg directions with respect to tensile axis notably changed with test temperature. The difference was caused by variant selection accompanying the $\gamma \rightarrow \alpha'$ transformation. At high temperatures, α' martensite formed only in the ~ 70 deg directions, where the mechanical driving force is large. At lower temperatures, however, α' martensite formed in the ~ 70 and 0 deg directions as well. It is also shown that stress/strain-induced ε martensite can only form in the ~ 70 deg directions. The results apply for all three examined steels.

https://doi.org/10.1007/s11661-020-05664-w

I. INTRODUCTION

STEELS exhibiting twinning-induced plasticity (TWIP) and transformation-induced plasticity (TRIP) are favored due to their unique combination of high stress and elongation. Their industrial processing involves shape giving, during which texture development and phase transformations occur simultaneously (besides other deformation mechanisms). Therefore, a detailed understanding of the underlying mechanisms and their interaction is of great importance. When austenite is mechanically deformed, crystallographic texture develops. When it undergoes transformation, the product phase (ferrite, acicular ferrite, bainite, ε martensite, α' martensite) is also textured. Since the crystal orientation of the new phase is obtained through phase transformation, the term ''transformation texture'' was introduced. Transformation texture is governed by the texture of prior austenite, the crystallographic correspondence between austenite and the product phase, and stress. While the first two determine all possible orientations of the new crystals, the latter specifies which orientations actually form among all. This is called ''variant selection''. Miyaji *et al.*[1] showed that variant selection acts simply due to geometrical non-uniformity even if external load is absent. Since then, the role of variant selection in different steel types has been recognized by many authors.[2–4] To predict the texture of the product phases, models had been established based on the observed $\{111\}_{\gamma}||\{011\}_{\alpha'}$, $\langle 1\bar{1}0\rangle_{\gamma}||\langle 1\bar{1}1\rangle_{\alpha'}$ orientation relations.[5–9] When it comes to describing the texture of austenite, difficulties arise. First, calculating the austenite texture is rather complicated, since one specific crystal orientation of the product phase can be inherited from multiple parent orientations.[2–4] This problem was resolved with promising results by the method of Tomida *et al.*[8] which specifies that the orientation relation of a nucleating ferrite and two adjoining austenite grains is fulfilled. Second, the texture of austenite can only be measured if there is a notable amount of retained austenite. In such case, it is possible to directly observe orientation relations between the parent and product phases. The orientation relationship between γ and α' phases[10] and texture evolution during tensile tests[11,12] or rolling and annealing[13–18] were studied by many authors. In some of these works, conclusions were deduced based on electron backscattered diffraction (EBSD) analysis,[10,11,15] while in others it was done on orientation distribution function (ODF) synthesis.[11–18] Both methods define texture through the orientation of unit cells, *i.e.*, texture components.[19,20] However, due to variant selection,

MARTON BENKE, ADRIENN HLAVACS, and VALERIA MERTINGER are with the Institute of Physical Metallurgy, Metalforming and Nanotechnology, University of Miskolc, Miskolc-Egyetemvaros 3515, Hungary. Contact e-mail: fembenke@uni-miskolc.hu ERZSEBET NAGY and GABOR KARACS are with the MTA-ME Materials Science Research Group, Miskolc-Egyetemvaros 3515, Hungary.

Manuscript submitted June 19, 2019.
Article published online February 4, 2020

martensite formations occur preferably on those $\gamma\{111\}$ planes—within an austenite unit cell—which are directed favorably with respect to applied stress or constraint stress.[1–4,21] On the macroscopic scale, consequently, a series of $\gamma\{111\}$ planes with favored orientations undergo transformation, while non-favored oriented planes do not. This predicts that due to variant selection, the resulting texture cannot be accurately characterized in terms of unit cell orientations. The aim of the present work is to describe the role of variant selection associated with deformation induced $\gamma \rightarrow \varepsilon$ and $\gamma \rightarrow \alpha'$ transformations in the final texture of TWIP/TRIP steels with different Cr content. At first, the case of uniaxial tensile loading is considered.

II. MATERIALS AND METHODS

Steels exhibiting both TWIP and TRIP behavior with Cr content of 0.07, 2.26 and 6.12 (wt pct) were produced and provided in the form of hot-rolled rods by the TU Bergakademie Freiberg. The compositions of the examined steels are given in Table I.

Cylindric tensile test specimens with diameter of 5 mm and samples for differential scanning calorimeter (DSC) examinations were machined from the hot-rolled rods. Afterwards, specimens were solution treated at 1273 K (1000 °C) in a resistance heating furnace under argon atmosphere for 30 minutes and subsequently quenched in room temperature water. According to XRD phase analysis, as-quenched (AQ) samples of all three steel types consisted of thermally induced ε martensite and γ austenite (Figure 1).

The $\varepsilon \leftrightarrow \gamma$ transformation temperatures were obtained with a Netzsch 204 heat flux DSC. The cylindric samples had 5 mm diameter and ~ 2 mm thickness. DSC scans were performed under Ar atmosphere using 10 K/min scan speed. The DSC curves and the determined transformation temperatures are shown in Figure 2. The $\varepsilon \leftrightarrow \gamma$ transformation temperatures are summarized in Table II. The start and finish temperatures refer to the $\varepsilon \leftrightarrow \gamma$ transformations.

Tensile tests were performed at different temperatures with an Instron 5982 universal mechanical tester equipped with a specimen furnace. Prior to loading, specimens were heated up to 573 K (300 °C) and held

Table I. Composition of the Examined Steels

	Composition, Wt Pct				
Steel Type	C	Mn	Cr	Si	S
Steel 0.07	0.028	18	0.07	0.03	0.025
Steel 2.26	0.026	17.7	2.26	0.1	0.029
Steel 6.12	0.08	17.7	6.12	0.06	0.025

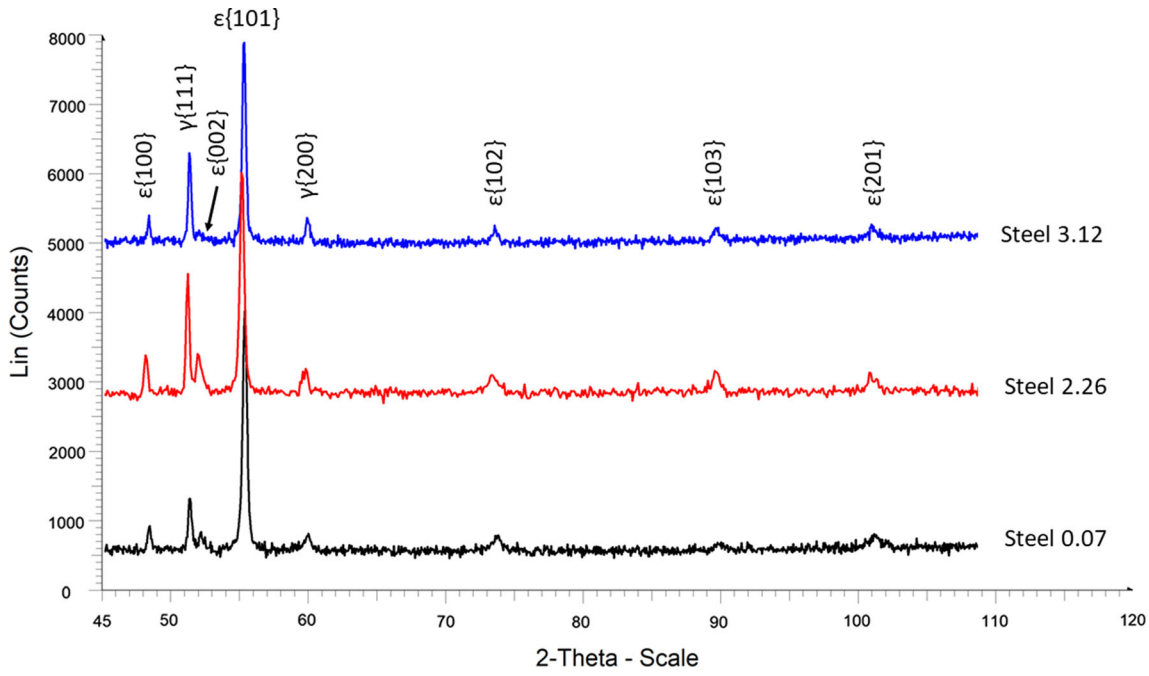

Fig. 1—XRD spectra of the as-quenched samples.

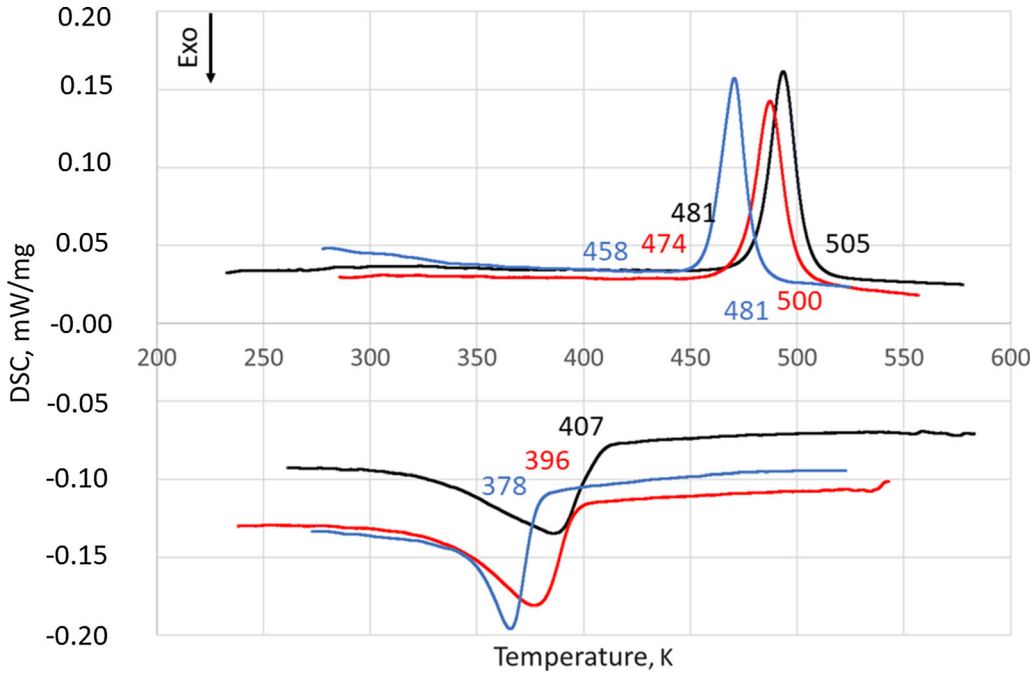

Fig. 2—DSC curves and transformation temperatures of the as-quenched samples.

Table II. The ε ↔ γ Transformation Temperatures of the As-Quenched Samples

Steel	M_s^{ε} K (°C)	A_s K (°C)	A_f K (°C)
Steel 0.07	407 (134)	481 (208)	505 (232)
Steel 2.26	396 (123)	474 (201)	500 (227)
Steel 6.12	378 (105)	458 (185)	481 (208)

for 30 minutes to obtain pure austenitic state. Afterwards, the specimens were cooled down to the test temperatures, namely: 473 K, 453 K, 433 K, 413 K, 398 K, 383 K (200 °C, 180 °C, 160 °C, 140 °C, 125 °C, 110 °C), and room temperature and they were loaded till fracture. Subsequently, cross-section samples were prepared from the gauge section of the tensile test specimens for transmission electron microscopy (TEM) and X-ray diffraction (XRD) texture examinations. Specimens for TEM examinations were prepared by ion beam milling. TEM examinations were carried out with a FEI Tecnai G2 equipment with ASTAR system. Samples were embedded in epoxy resin and mechanically polished. XRD measurements were carried out with a Bruker D8 Advance type diffractometer equipped with Eulerian cradle and CoKα X-ray source, operating with 40 kV tube voltage and 40 mA tube current. The length of the applied line focus was 20 mm while its width was a few mm depending on the Bragg-angle, meaning that the full cross-section of the samples were examined during measurements. Incomplete pole figures were measured to $\theta = 75$ deg tilting and were defocus corrected. Figure 3. shows the diffracting {hkl} plane series with a general orientation within a cylindrical sample. Here, θ is the angle between the normal of the {hkl} plane series (N) and the direction of applied stress (σ_1). On the presented pole figures, the center of the pole figures ($\theta = 0$ deg) correspond to the axis of applied stress (σ_1) and θ increases radially.

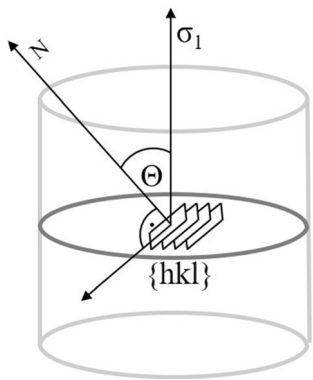

Fig. 3—The diffracting {hkl} plane series within a cylindrical specimen. θ is the angle between the normal of the {hkl} plane series (N) and the direction of applied stress (σ_1).

Recalculated pole figures were obtained using the harmonic method and positivity refinement.[19,22] Orientation distribution functions (ODF) were calculated with the equipment's own software, TexEval. From the data of pole figures, the ratio of net intensity at the $\theta = 70$ deg directions (summarized from 50 to 75 deg)

and at $\theta = 0$ deg direction (from 0 to 20 deg) of $\gamma\{111\}$ and $\alpha'\{110\}$ pole figures were calculated ($Z_{\gamma\{111\}}$ and $Z_{\alpha'\{110\}}$, respectively). Note that on the 111 standard projection, 1 pole is at $\theta = 0$ deg and 3 poles can be found at $\theta = 70$ deg.[20] Thus, the theoretical value of $Z_{\gamma\{111\}}$ is 3 in the case of $\langle 111 \rangle$ fiber texture if variant selection does not take place. *Vice versa*, notably different values for $Z_{\gamma\{111\}}$ suggest that variant selection took place. In addition, the value of Z is close to 1 for all $\langle hkl \rangle$ poles in the case of a randomly oriented structure.

III. RESULTS

Figure 4 shows the true stress–true strain curves of the steel tensile tested at different temperatures.

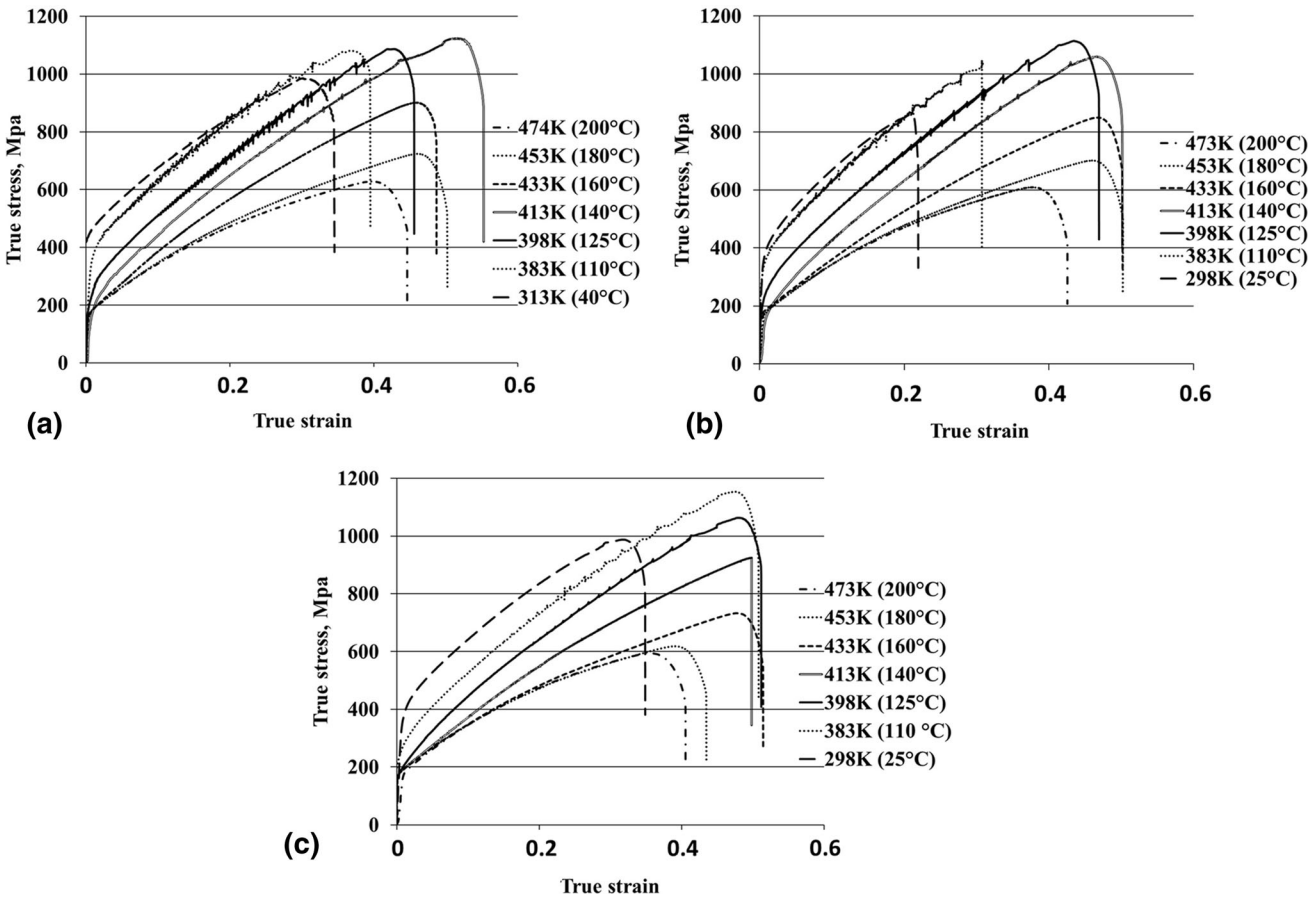

Fig. 4—True stress-true strain curves obtained at different temperatures from the examined steels (*a*) Steel 0.07, (*b*) Steel 2.26[23] and (*c*) Steel 6.12.

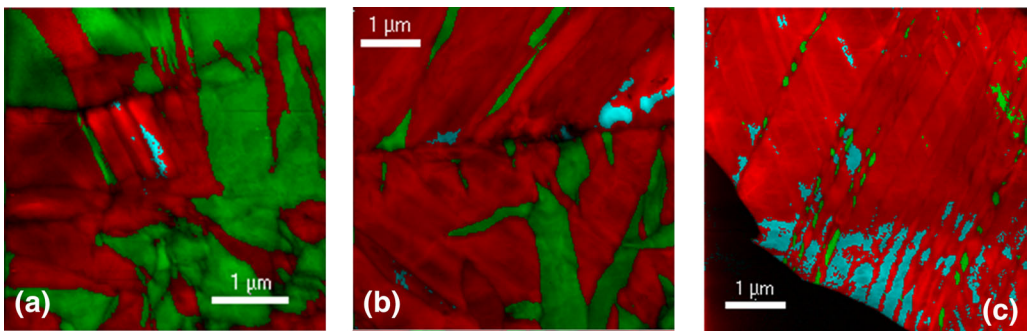

Fig. 5—Cross-section TEM phase maps of (*a*) Steel 0.07, (*b*) Steel 2.26 and (*c*) Steel 6.12 tensile tested at 398 K (125 °C). Cyan: γ austenite, red: ε martensite, green: α' martensite (Color figure online).

According to XRD phase analysis, tensile-tested samples consisted of austenite, ε martensite and α′ martensite.

In Figure 5, TEM phase maps taken from the cross-section of Steel 0.07 (Figure 5(a)), Steel 2.26 (Figure 5(b)) and Steel 6.12 (Figure 5(c)) tensile tested at 398 K (125 °C) can be seen. On the images, cyan-colored areas correspond to austenite, red corresponds to ε martensite and green to α′ martensite. Note that the examined volume is too small to give reliable information about the relative amount of the present phases.

A. *Texture*

Figure 6 shows the sections of the obtained XRD plots from which the Bragg angles of the γ{111}, ε{002} and α′{110} reflections were determined. The relative

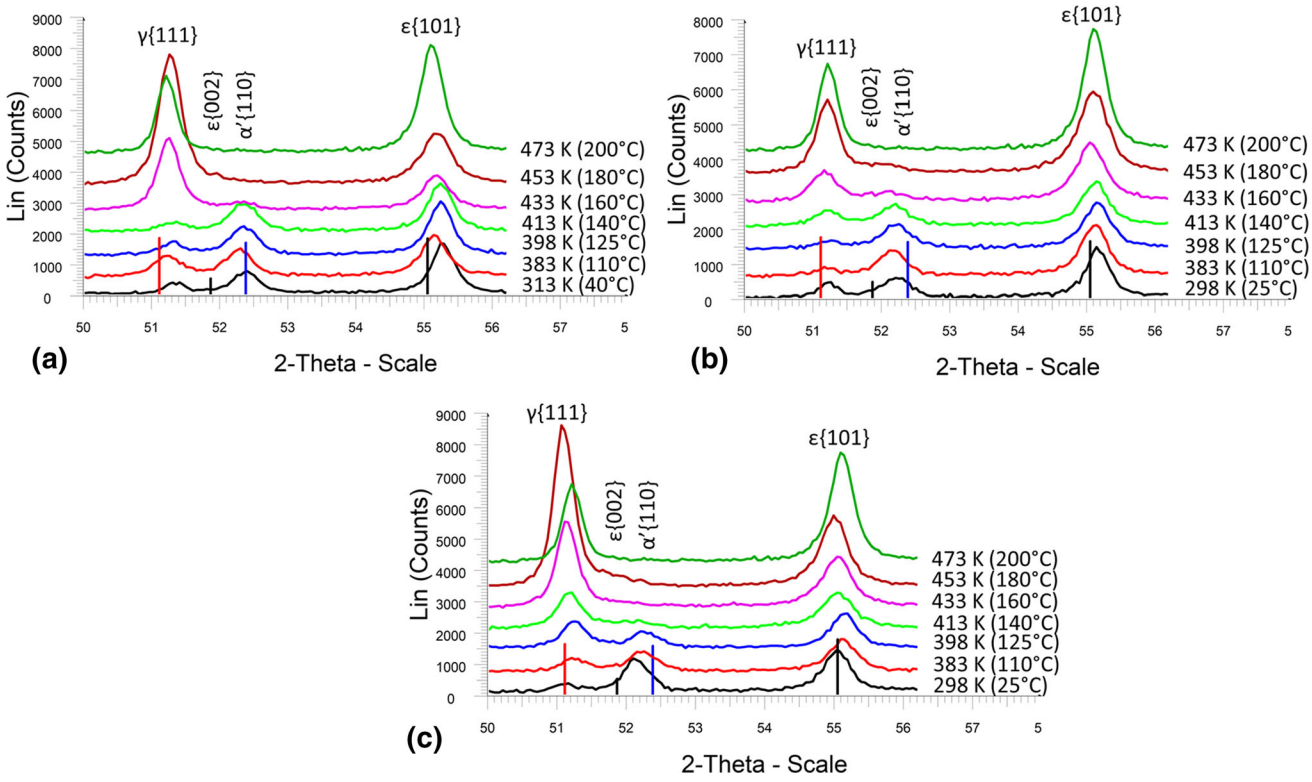

Fig. 6—XRD plots obtained at different temperatures from the examined steels (*a*) Steel 0.07, (*b*) Steel 2.26 and (*c*) Steel 6.12.

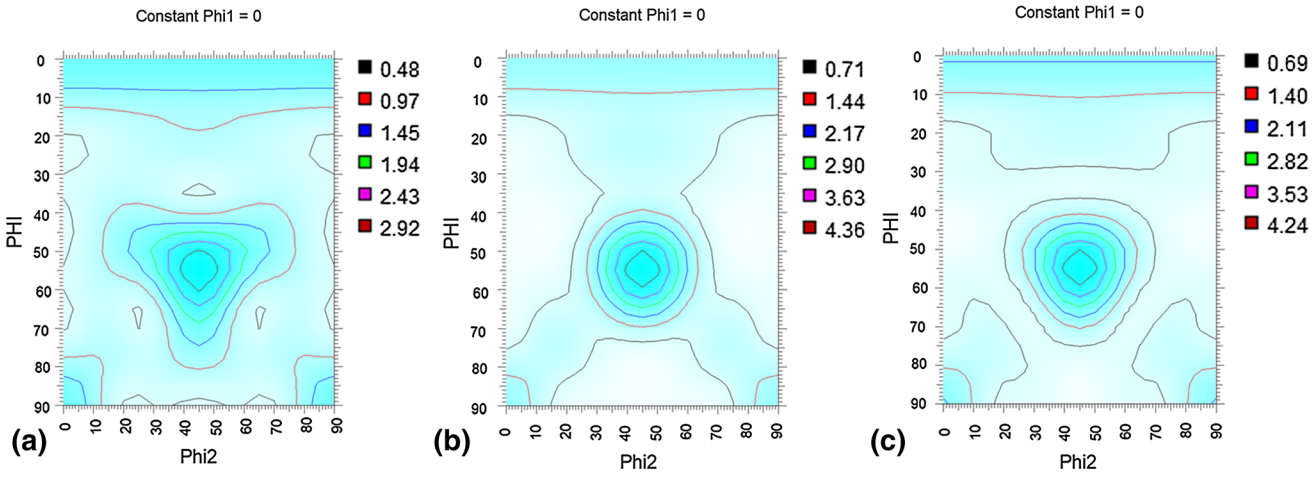

Fig. 7—The PHI1 = 0 ODF cuts of the γ phase, obtained from of (*a*) Steel 0.07, (*b*) Steel 2.26 and (*c*) Steel 6.12 tested at 453 K.

heights of the reflections change with test temperature due to the developing texture of the phases.

The developed fiber texture of the γ phase is clearly seen on the PHI = 0 deg ODF cuts taken from the steels tested at 453 K (Figure 7).

Figure 8 shows the measured $\gamma\{111\}$ (a, d, g, j, m, p), $\varepsilon\{002\}$ (b, e, h, k, n, q) and $\alpha'\{110\}$ (c, f, I, l, o, r) XRD pole figures of the steel tensile tested at different temperatures. Pole density (measured intensity) is proportional to the color saturation of the pole figures.

In Figures 8(a), (g) and (m), it can be seen that at 473 K (200 °C), the $\gamma\{111\}$ poles appear at $\theta \approx 0$ deg and at $\theta \approx 70$ deg. The poles at $\theta \approx 0$ deg are from those $\gamma\{111\}_{\theta = 0 \text{ deg}}$ planes that are closely parallel with the cross-section (perpendicular to the tensile axis), while poles at $\theta \approx 70$ deg are tilted with 70 deg relative to the

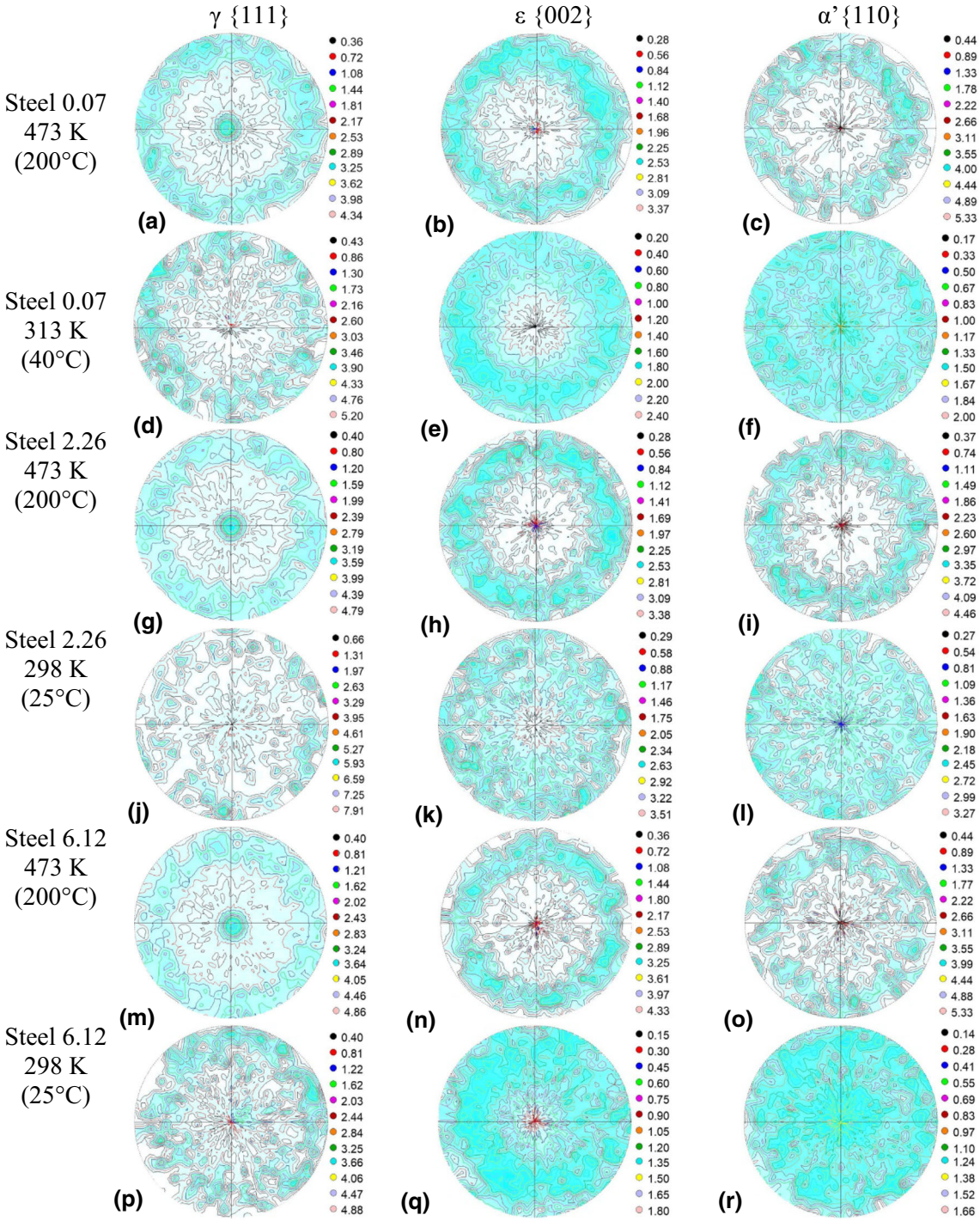

Fig. 8—Measured $\gamma\{111\}$ (*a*, *d*, *g*, *j*, *m*, *p*), $\varepsilon\{002\}$ (*b*, *e*, *h*, *k*, *n*, *q*) and $\alpha'\{110\}$ (*c*, *f*, *i*, *l*, *o*, *r*) pole figures of Steel 0.07, Steel 2.26 and Steel 6.12 tensile tested at 473 K (200 °C) and at room temperature (Color figure online).

tensile axis. In other words, the $\gamma\langle 111\rangle$ fiber texture formed during tensile loading which is in agreement with the literature. However, at 473 K (200 °C), the pole densities are high at $\theta \approx 0$ deg and low at $\theta \approx 70$ deg, while at room temperature (313 K and 298 K, they are high at $\theta \approx 70$ deg, and low at $\theta \approx 0$ deg (Figures 8(d), (j), and (p)). On the $\varepsilon\{002\}$ pole figures taken from 473 K (200 °C) high pole densities can only be observed at $\theta \approx 70$ deg directions, and more uniform distributions are found at room temperature (313 K and 298 K, Figures 8(b), (h), (n) and (e), (k), (q), respectively). In Figures 8(c), (i), and (o), the $\alpha'\{110\}$ pole figures from 473 K (200 °C) also have high pole densities at the $\theta \approx 70$ deg directions. At 313 K and 298 K (40 °C and 25 °C), however, the pole distributions are completely random (Figures 8(f), (l), and (r)). The above shown pole figures correspond to the highest and the lowest test temperatures and provide only qualitative information about the pole distributions. To quantitatively show the pole density variation of γ and α' phases in the whole temperature range of all three steels, the ratio (Z) of measured intensity at $\theta \approx 70$ deg and $\theta \approx 0$ deg of $\gamma\{111\}$ and $\alpha'\{110\}$ pole figures for all three steels are shown in Figure 9.

As seen in Figure 9, both $Z_{\gamma\{111\}}$ and $Z_{\alpha'\{110\}}$ strongly vary with test temperature. In the case of Steel 0.07, the theoretical value of 3 is obtained for $Z_{\gamma\{111\}}$ below 413 K (Figure 9(a)). This means that $Z_{\gamma\{111\}}$ is identical to the 111 standard projection. However, $Z_{\gamma\{111\}}$ decreases from 400 K and goes below 1 at high temperatures. The value below 3 means that within the $\langle 111\rangle$ textured austenite unit cells, the ~ 70 deg oriented $\gamma\{111\}_{\theta = 70\ \mathrm{deg}}$ planes underwent phase transformation, while the $\gamma\{111\}_{\theta = 0\ \mathrm{deg}}$ planes did not. For the other two steels, $Z_{\gamma\{111\}}$ is between 3 and 1 at low temperatures suggesting that more $\gamma\{111\}_{\theta = 70\ \mathrm{deg}}$ planes transformed than $\gamma\{111\}_{\theta = 0\ \mathrm{deg}}$ planes. At higher temperatures, similarly to Steel 0.07, $Z_{\gamma\{111\}}$ decreases below 1. For α' martensite, $Z_{\alpha'\{110\}}$ is notably larger than 1 at high temperatures and it is around 1 at low temperatures. Accordingly, at high temperatures, $\alpha'\{110\}$ planes are dominantly parallel with the ~ 70 deg directions and are randomly oriented at low temperatures. $Z_{\varepsilon\{002\}}$ was not calculated since thermally induced ε (with random orientations) also could form (thermally formed ε was present at some test temperatures) besides the stress/strain-induced ε. Furthermore, it will be shown later that

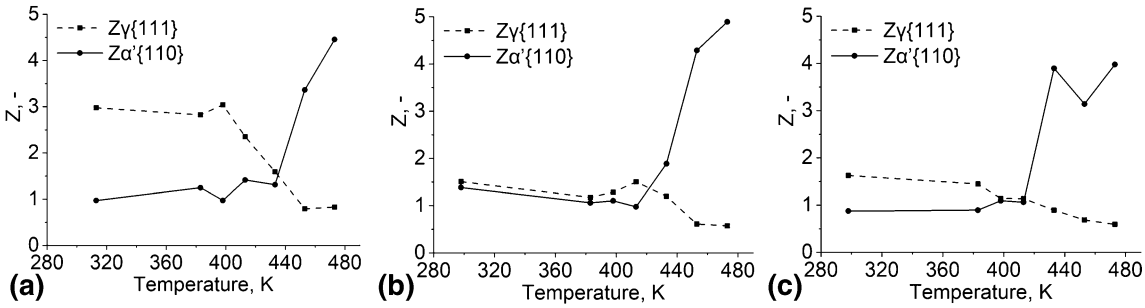

Fig. 9—Net intensity ratio (Z) of the ~ 70 and 0 deg directions of the $\gamma\{111\}$ and $\alpha'\{110\}$ pole figures *vs* test temperature of (*a*) Steel 0.07, (*b*) Steel 2.26 and (*c*) Steel 6.12.

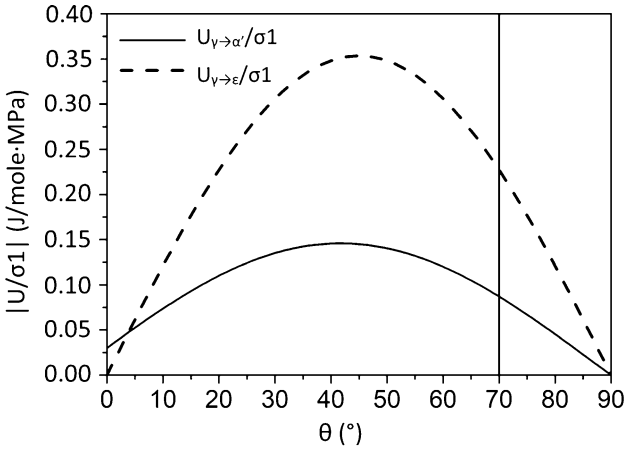

Fig. 10—The absolute value of mechanical driving force (U) of the $\gamma \rightarrow \alpha'$ and $\gamma \rightarrow \varepsilon$ transformations per applied stress (σ_1) *vs* the angle between tensile direction and normal of the habit plane (θ).

theoretically stress/strain-induced ε martensite can only form at $\gamma\{111\}_{\theta = 70\ \text{deg}}$ planes.

IV. DISCUSSION

To understand the fine details of the developed texture, the effect of variant selection accompanying the occurring phase transformations are taken into account. To introduce the contribution of external stress to martensitic transformations, the mechanical driving force (U) of the $\gamma \rightarrow \alpha'$ and $\gamma \rightarrow \varepsilon$ transformations were calculated according to (1) after Patel and Cohen[5] and Seetharaman,[24] where σ_1 is the applied stress, δ is the dilatation component and s is the shear component of the transformation deformation. For the $\gamma \rightarrow \alpha'$ transformation, values of $\delta = 0.03$ and $s = 0.26$ were used,[21] while in the case of $\gamma \rightarrow \varepsilon$, the transformation deformation is a simple shear with $\delta = 0$ and $s = 1/\sqrt{2}$.[25] The dependency of U on θ is plotted in Figure 10.

$$U = \frac{\sigma_1}{2}(\delta + \delta\cos 2\theta + s\sin 2\theta). \qquad [1]$$

In Figure 10, it can be seen that both $U_{\gamma \rightarrow \alpha'}/\sigma_1$ and $U_{\gamma \rightarrow \varepsilon}/\sigma_1$ are maximal at $\theta \approx 45$ deg. However, since the austenite phase developed a $\langle 111\rangle$ texture, habit planes are only available at the $\theta = 0$ deg and $\theta \approx 70$ deg orientations. From Figure 10, it is also apparent that $U_{\gamma \rightarrow \alpha'}/\sigma_1$ is almost 3 times larger at $\theta \approx 70$ deg (0.087) than at $\theta \approx 0$ deg (0.030). According to this, stress/strain-induced α' martensite plates form preferably on $\gamma\{111\}_{\theta = 70\ \text{deg}}$ planes at higher temperatures, where the chemical driving force is weak.[24] As the $\gamma\{111\} \rightarrow \alpha'\{110\}$ transformation occurred along the $\gamma\{111\}_{\theta = 70\ \text{deg}}$ planes, the $\gamma\{111\}_{\theta \approx 70\ \text{deg}}$ pole density decreased, while that of $\alpha'\{110\}_{\theta \approx 70\ \text{deg}}$ increased. (Consequently, $Z_{\gamma\{111\}}$ decreased while $Z_{\alpha'\{110\}}$ increased.) At low temperatures, where the chemical driving force is increased, the $\gamma \rightarrow \alpha'$ transformation was activated also on the $\gamma\{111\}_{\theta = 0\ \text{deg}}$ planes where the mechanical contribution is weaker. In that case, $\gamma \rightarrow \alpha'$ transformation occurred in both $\gamma\{111\}_{\theta = 70\ \text{deg}}$ and $\gamma\{111\}_{\theta = 0\ \text{deg}}$ planes. Consequently, $\gamma\{111\}$ pole density is decreased and $\alpha'\{110\}$ poles appear at both $\theta \approx 0$ deg and $\theta \approx 70$ deg directions. In the case of ε martensite, $U_{\gamma \rightarrow \varepsilon}/\sigma_1$ is notable at $\theta \approx 70$ deg (0.227) and it is 0 at $\theta = 0$ deg. Thus, stress/strain-induced ε formation can occur only on $\gamma\{111\}_{\theta = 70\ \text{deg}}$ habit planes, regardless of test temperature. Therefore, stress/strain-induced ε $\{002\}$ poles appear only at $\theta \approx 70$ deg. (Note that ε can also form thermally without any preferred orientation.) It was also seen that for Steel 0.07, the theoretical pole distribution of the 111 standard projection was obtained at low temperatures, while this was not the case for Steel 2.26 and Steel 6.12. This can be the result of two factors. First, M_s^{ε} is the highest of Steel 0.07 (407 K compared to 396 K and 378 K). Thus, it can be assumed that most thermally induced, randomly oriented ε and consequently, the least stress/strain induced, $\langle 002\rangle_{\theta = 70\ \text{deg}}$ oriented ε formed in the 0.07 pct Cr steel compared to the other two. As a result, the effect of the $\gamma\{111\}_{\theta = 70\ \text{deg}} \rightarrow \{002\}_{\theta = 70\ \text{deg}}$ transformation on the $\gamma\{111\}_{\theta = 70\ \text{deg}}$ pole density was the least pronounced in Steel 0.07. Second, the effect of Cr content on the stacking fault energy could play a role in the texture development. This, however, needs further investigation.

V. SUMMARY

After uniaxial tensile tests performed at different temperatures on steels with varying Cr content showing TWIP/TRIP behavior it was shown that the $\gamma\langle 111\rangle$ and $\alpha'\langle 110\rangle$ fiber texture developed and the $\gamma\{111\} \parallel \varepsilon\{001\} \parallel \alpha'\{011\}$ crystallographic correlation (more precisely, close to the $\gamma\{111\} \parallel \alpha'\{011\}$ correlation) was observed which is in agreement with the literature.[5–9] However, notable differences were observed in diffracted $\gamma\{111\}$ and $\alpha'\{110\}$ intensities between the $\theta = 70$ deg and $\theta = 0$ deg directions at various test temperatures. The mechanical contribution of the stress/strain-induced $\gamma \rightarrow \varepsilon$ and the $\gamma \rightarrow \alpha'$ transformations were calculated and it was concluded that the observed intensity differences are caused by variant selection which accompanies the stress/strain-induced $\gamma \rightarrow \varepsilon$ and $\gamma \rightarrow \alpha'$ transformations. It is shown that at higher temperatures, α' martensite plates form preferably on $\gamma\{111\}$ planes that are oriented $\theta \approx 70$ deg with respect to the tensile direction, while at lower temperatures, plates form on all available $\gamma\{111\}$ planes. It is also shown that stress/strain-induced ε martensite can only form on $\theta \approx 70$ deg $\gamma\{111\}$ planes, while thermally induced ε forms on every available $\gamma\{111\}$ planes.

ACKNOWLEDGMENTS

Open access funding provided by University of Miskolc (ME). The authors are grateful for TU Bergakademie Freiberg for the raw material provided. The paper was supported by the János Bolyai Research Scholarship of the Hungarian Academy of Sciences. Thermomechanical treatments were performed within the GINOP-2.3.2-15-2016-00027 project and funded by the European Union and the European Regional Development Fund. Texture examinations were carried out within the NKFIH K119566 project and funded by the National Research, Development and Innovation Office.

REFERENCES

1. H. Miyaji and E. Furubayashi: *Texture Microstruct*., 1991, vols. 14–18, pp. 561–66.
2. J. Savoie, R.K. Ray, M.P. Butron-Guillen, and J.J. Jonas: *Acta Metall. Mater*., 1994, vol. 42, pp. 2511–23.
3. R.K. Ray, J.J. Jonas, M.P. Butron-Guillen, and J. Savoie: *ISIJ Int*., 1994, vol. 34, pp. 927–42.
4. N. Gey, B. Petit, and M. Humbert: *Metall. Mater. Trans. A*, 2005, vol. 36A, pp. 3291–99.
5. J.R. Patel and M. Cohen: *Acta Metall*., 1953, vol. 1, pp. 531–38.
6. S. Kundu and H.K.D.H. Bhadeshia: *Scripta Mater*., 2006, vol. 55, pp. 779–81.
7. H.K.D.H. Bhadeshia and R.W.K. Honeycombe: *Steels Microstructure and Properties*, 3rd ed., Elsevier, Amsterdam, 2006, pp. 111–12.
8. T. Tomida and M. Wakita: *ISIJ Int*., 2012, vol. 52, pp. 601–09.
9. A. Matsumoto, M. Chen, A. Shibata, T. Miyazawa, M. Sato, and N. Tsuji: *Mater. Today: Proc*., 2015, vol. 2S, pp. S945–48.
10. F. Lu, P. Yang, L. Meng, F. Cui, and H. Ding: *J. Mater. Sci. Technol*., 2011, vol. 27, pp. 257–65.
11. D. Barbier, N. Gey, S. Allain, N. Bozzlo, and M. Humbert: *Mat. Sci. Eng. A*, 2009, vol. 500, pp. 196–206.
12. X. Fang, P. Yang, F. Lu, and L. Meng: *J. Iron Steel Res. Int*., 2011, vol. 18, pp. 46–52.
13. S. Vercammen, B. Blanpain, B.C. De Cooman, and P. Wollants: *Acta Mater*., 2004, vol. 52, pp. 2005–12.
14. L. Bracke, K. Verbeken, L. Kestens, and J. Penning: *Acta Mater*., 2009, vol. 57, pp. 1512–24.
15. Y. Lü, B. Hutchinson, D.A. Molodov, and G. Gottstein: *Acta Mater*., 2010, vol. 58, pp. 3079–90.
16. Y. Lü, D.A. Molodov, and G. Gottstein: *ISIJ Int*., 2011, vol. 51, pp. 812–17.
17. A.A. Saleh, E.V. Pereloma, and A.A. Gazder: *Mat. Sci. Eng. A*, 2011, vol. 528, pp. 4537–49.
18. M. Ashiq, P. Dhekne, A.S. Hamada, P. Sahu, B. Mahato, R.K. Minz, S.G. Chowdhury, and L.P. Karjalainen: *Metall. Mater. Trans. A*, 2017, vol. 48 (10), pp. 4842–56.
19. O. Engler and V. Randle: *Introduction to Texture Analysis*, 2nd ed., CRC Press, Boca Raton, 2010, pp. 208–13.
20. S. Suwas and R.K. Ray: *Crystallographic Texture of Materials*, Springer, Berlin, 2014, p. 13.
21. H.K.D.H. Bhadeshia: *ISIJ Int*., 2002, vol. 42, pp. 1059–60.
22. Bruker AXS GmbH: Texeval Texture Evaluation Program Version 2.4 User's Manual, Bruker AXS GmbH, 2002, pp. 33–41.
23. M Sepsi, A. Talgotra, E. Nagy, M. Benke, V. Mertinger: *Proc. MultiSci.: XXXI. microCAD Int. Multidiscip. Sci. Conf*. (2017) ISBN 978-963-358-132-2.
24. V. Seetharaman: *Bull. Mater. Sci*., 1984, vol. 6, pp. 703–16.
25. B. Qin and H.K.D.H. Bhadeshia: *Mater. Sci. Technol*., 2008, vol. 24, pp. 969–73.